LA-UR-21-20842

Approved for public release; distribution is unlimited.

Title:	GnarlyX: Eulerian multi-material hydrodynamics coupled to equation of state and hyperelastic, plastic constitutive models
Author(s):	Cheng, Roseanne Marie Aslam, Tariq Dennis Luscher, Darby Jon Ticknor, Christopher
Intended for:	Report
Issued:	2023-03-24 (rev.2)

LA-UR-21-20842

GnarlyX: Eulerian multi-material hydrodynamics coupled to equation of state and hyperelastic, plastic constitutive models

Roseanne M. Cheng,* Tariq D. Aslam,† D. J. Luscher,‡ and Chris Ticknor§

Los Alamos National Laboratory

P.O. Box 1663

Los Alamos, NM 87545 (USA)

(Dated: March 14, 2023)

Abstract

GnarlyX is a new hydrocode for direct numerical simulations of the microstructural behavior of high explosives at the mesoscale. We summarize the computational framework for multi-dimensional, Eulerian multi-material hydrodynamics coupled to EOS and hyperelastic, plastic constitutive models. We present 1D verification tests of multi-material only and combined multi-material and strength capabilities with comparisons to exact solutions of shock states resulting from an incident shock impacting the material interface of PBX9502 and aluminum. We show that GnarlyX performs well in capturing the resulting shock waves in examining numerical convergence with exact solutions. In later work, we will summarize the thermomechanics and multi-dimensional, parallel computing capabilities in GnarlyX with multi-dimensional verification tests.

CONTENTS

* rmcheng@lanl.gov; Fluid Dynamics and Solid Mechanics (T-3)

† aslam@lanl.gov; Physics and Chemistry of Materials (T-1)

‡ djl@lanl.gov; Fluid Dynamics and Solid Mechanics (T-3)

§ cticknor@lanl.gov; Physics and Chemistry of Materials (T-1)

I. INTRODUCTION

In this technical report, we present GnarlyX, a new hydrocode for investigating the leading mechanisms of initiation in high explosives (HE). This computational framework enables high fidelity thermomechanics in simulating the complex behavior of energetic materials. High explosive plastic bonded explosives (PBX) are heterogeneous materials consisting of brittle explosive crystals with a polymeric binder [1]. Macroscopic performance depends on the microstructural constituents because even small microscopic changes lead to distinct behavior [2, 3]. Internal defects such as porosity, interfaces, and cracks initiate reactions while thermal conductivity, the underlying chemical reaction rates, and exothermicity control burn. The interplay of these features and mechanisms represents the thermochemistry at the chemical reaction zone ($\sim$100 microns). A critical barrier to understanding the leading mechanisms of initiation in HE is bridging the microscopic and macroscopic length and time scales, via the mesoscales. GnarlyX is a new hydrocode designed to address this challenge through direct numerical simulations (DNS) at the mesoscale, providing representative details that inform multi-scale, thermochemistry in HE burn. GnarlyX is computed with Eulerian frame multi-physics hydrodynamics to ensure a robust, computational mesh treatment in modeling these large deformation mechanics systems. The multi-physics capabilities include multi-material hydrodynamics for the shock response, compaction of voids, and elastic-plastic strength, as well as constitutive models for the equation of state (EOS), chemical reactions, anisotropic crystal plasticity, and thermal conduction. This technical report focuses on the multi-material and strength capabilities of GnarlyX. While the ver-

ification test presented here is at the macroscale, the capabilities are also applicable to the mesoscale. In Sec. II, we summarize the computational framework for multi-dimensional, Eulerian multi-material hydrodynamics coupled to EOS and hyperelastic, plastic constitutive models in GnarlyX. This framework is based on a conservative, hyperbolic system for finite deformation [4–10] and a ghost fluid method for multi-materials [11–14]. By construction, it is thermodynamically consistent in terms of a Helmholtz free energy. The hydrodynamic update is straightforward to implement using high resolution shock capturing methods [15]. The base infrastructure of GnarlyX is the parallel computing, hydrodynamics framework of Athena++, an open source, multi-dimensional, Eulerian hydrodynamics code for astrophysical fluid dynamics [16–19]. The changes from Athena++ to GnarlyX are the significant modifications and additions in implementing a new numerical scheme for multi-material evolution of condensed phase EOS and hyperelastic plastic constitutive models. Thus, this work brings the base infrastructure from a hydrodynamics code to a *hydrocode*, for simulating hydrodynamics and solid motion. These differences include new evolution equations, Riemann solvers, wave speed calculations, source terms, EOS and material strength models, data structures, and parallel computing communication (MPI) networks. In GnarlyX, the material deformation manifests as a Cauchy stress field where the deformation field itself is identified as an evolving transformation between Eulerian and Lagrangian frames. This frame transformation enables an implementation of plasticity models, such as crystal plasticity, used previously in Lagrangian and Lagrangian-Eulerian (ALE) schemes [20–22]. In Sec. III, we showcase 1D verification tests of multi-material only and combined multi-material and strength capabilities, in comparing numerical results of GnarlyX to exact solutions. In Sec. IV, we summarize the results in this report. In later work, we will showcase the thermomechanics and multi-dimensional, parallel computing capabilities in GnarlyX with multi-dimensional verification tests.

II. GOVERNING EQUATIONS

A. Hydrodynamics coupled to constitutive equations

Consider the hydrodynamic evolution of a single material, governed by the mass, momentum, and energy conservation laws in Cartesian coordinates. In Eulerian form, we have

$$\frac{\partial \rho}{\partial t} + \frac{\partial}{\partial x_i}\left(\rho u_i\right) = 0, \tag{1}$$

$$\frac{\partial \rho u_i}{\partial t} + \frac{\partial}{\partial x_j}\left(\rho u_i u_j - \sigma_{ij}\right) = 0, \tag{2}$$

$$\frac{\partial \rho e_{\text{tot}}}{\partial t} + \frac{\partial}{\partial x_i}\left(\rho e_{\text{tot}} u_i - \sigma_{ij} u_j\right) = 0, \tag{3}$$

with density ρ, velocity $\vec{u}$, Cauchy stress σ, and specific total energy e_{tot}. The specific total energy is given in terms of the internal energy e_{eos} from the EOS, internal elastic energy e_{elastic} from the constitutive model, and kinetic energy $e_k = \frac{1}{2} u_i u_i$, where

$$e_{\text{tot}} = e_{\text{eos}} + e_{\text{elastic}} + e_k. \tag{4}$$

The constitutive model is described by the deformation gradient tensor $\mathbf{F}$, defined in component form as $F_{ij} = \partial x_i / \partial X_j$, the coordinate transformation between the Eulerian x_i and Lagrangian X_j frames. We define the Cauchy stress σ and specific internal energies (per mass) e_{eos} and e_{elastic} in terms of a Helmholtz free energy state function,

$$\Psi(V, \mathbf{F}, T) = \Psi_{\text{eos}}(V, T) + \Psi_{\text{elastic}}(\mathbf{F}, T), \tag{5}$$

for specific volume V, temperature T, and deformation gradient tensor $\mathbf{F}$, with separable contributions from the EOS, Ψ_{eos}, and deviatoric contributions which represent material strength, Ψ_{elastic}. The specific internal energy (including both EOS and deviatoric parts), in terms of the Helmholtz free energy, is given by

$$e_{\text{int}} = \Psi - T\frac{\partial \Psi}{\partial T} = e_{\text{eos}} + e_{\text{elastic}}. \tag{6}$$

The Cauchy stress is then

$$\sigma_{ij} = \frac{\rho F_{ik}}{\det \mathbf{F}} \frac{\partial \Psi}{\partial F_{jk}}. \tag{7}$$

Additionally, the Cauchy stress may be separated into components of pressure p from the EOS and deviatoric stress τ from the constitutive model, where

$$\sigma_{ij} = -\delta_{ij} p + \tau_{ij}. \tag{8}$$

The total deformation gradient is defined through the multiplicative decomposition $\mathbf{F} = \mathbf{F}^e\mathbf{F}^p$, with elastic $\mathbf{F}^e$ and plastic $\mathbf{F}^p$ contributions. For elastic-plastic strength [6, 7, 10, 14], we couple the conservation laws Eq. 1-3 to the conservative evolution equation for the elastic deformation gradient $\mathbf{F}^e$,

$$\frac{\partial}{\partial t}(\rho F^e_{ij}) + \frac{\partial}{\partial x_k}(u_k \rho F^e_{ij} - u_i \rho F^e_{kj}) = -u_i \frac{\partial}{\partial x_k}(\rho F^e_{kj}) - \rho \Omega^p_{ij}, \tag{9}$$

where total energy e_{tot}, stress σ, and plastic source term $\mathbf{\Omega}^p$ are defined in terms of $\mathbf{F}^e$ for a given elasticity/plasticity model. We specify the evolution in terms of the elastic deformation gradient $\mathbf{F}^e$ instead of the total deformation gradient $\mathbf{F}$ as the plastic part $\mathbf{F}^p$ does not contribute to the stress and energy. Specifically, it is not thermodynamically admissible to use the plastic deformation gradient tensor as a state variable because it lacks a "one-to-one" connection with the material state.

B. Wave speeds for hydrodynamics with strength

We obtain the hydrodynamic wave speeds by re-casting the conservative system given in Eqs. 1, 2, 3, and 9, for purely elastic behavior (no sources), in quasi-linear form [23, 24], as

$$\frac{\partial \mathcal{U}}{\partial t} + \frac{\partial \mathcal{F}^k(\mathcal{U})}{\partial \mathcal{U}} \frac{\partial \mathcal{U}}{\partial x^k} = \frac{\partial \mathcal{U}}{\partial t} + \mathbf{A}^k(\mathcal{U}) \frac{\partial \mathcal{U}}{\partial x^k} = 0. \tag{10}$$

Note that the matrix $\mathbf{A}^k(\mathcal{U})$ is in terms of the conservative variables $\mathcal{U}$. In multi-dimensions, we consider the wave speeds separately, splitting the quasi-linear system of Eq. 10. For the x-direction, where $\mathbf{A}(\mathcal{U}) = \partial \mathcal{F}^k(\mathcal{U})/\partial \mathcal{U}$, we have

$$\frac{\partial \mathcal{U}}{\partial t} + \mathbf{A}(\mathcal{U}) \frac{\partial \mathcal{U}}{\partial x} = 0. \tag{11}$$

We re-cast $\mathbf{A}$, for convenience, in terms of conservative variables ξ_k,

$$\mathcal{U} = \begin{pmatrix} \xi_1 \\ \xi_2 \\ \xi_3 \\ \xi_4 \\ \xi_5 \\ \xi_6 \\ \xi_7 \\ \xi_8 \\ \xi_9 \\ \xi_{10} \\ \xi_{11} \\ \xi_{12} \\ \xi_{13} \\ \xi_{14} \end{pmatrix} = \begin{pmatrix} \rho \\ \rho u_1 \\ \rho u_2 \\ \rho u_3 \\ \rho e_{\text{tot}} \\ \rho F^e_{11} \\ \rho F^e_{12} \\ \rho F^e_{13} \\ \rho F^e_{21} \\ \rho F^e_{22} \\ \rho F^e_{23} \\ \rho F^e_{31} \\ \rho F^e_{32} \\ \rho F^e_{33} \end{pmatrix}. \tag{12}$$

Note that the Cauchy stress is dependent on a subset of the conservative variables ξ_k,

$$\sigma = \sigma(\xi_1, \xi_6, \xi_7, \xi_8, \xi_9, \xi_{10}, \xi_{11}, \xi_{12}, \xi_{13}, \xi_{14}). \tag{13}$$

We then have $\mathbf{A}$, for the x-direction, obtained from calculating the derivatives of the flux $\mathcal{F}^x$, with respect to ξ_k such that

$$\mathbf{A} = \begin{pmatrix} \frac{\partial \mathcal{F}^x_{11}}{\partial \xi_1} & \cdots & \frac{\partial \mathcal{F}^x_{11}}{\partial \xi_{14}} \\ \vdots & & \vdots \\ \frac{\partial \mathcal{F}^x_{14}}{\partial \xi_1} & \cdots & \frac{\partial \mathcal{F}^x_{14}}{\partial \xi_{14}}. \end{pmatrix} \tag{14}$$

The eigenvalues of $\mathbf{A}$ are,

$$\{0, 0, 0, u_1, u_1, u_1, u_1, u_1, u_1, u_1, u_1 + c_{\text{long}}, u_1 - c_{\text{long}}, u_1 + c_{\text{shear}}, u_1 - c_{\text{shear}}\}, \tag{15}$$

for the longitudinal c_{long} and shear c_{shear} wave speeds. A similar procedure is used to obtain the wave speeds in the y- and z-directions.

C. Multi-material evolution with level set functions

We track multiple regions of materials using level set functions in order to place spatial limits on the multi-material evolution. A level set $\Phi(\vec{x}, t)$ is a smooth signed distance function

which gives values for the shortest distance to the interface [13]. For $\Phi^m < 0$, $\vec{x}$ is inside the region of material m. For $\Phi^m > 0$, $\vec{x}$ is outside the region of material m. For $\Phi^m = 0$, $\vec{x}$ is at the interface location, the material boundary. For the update, we consider a set of variables for each material, represented by m, where $m = 0, \ldots, N-1$, for N number of materials in the computational domain. In GNARLYX, we implement the level set evolution described in Osher *et al.* [13]. The level set evolves as a convection / advection equation,

$$\frac{\partial \Phi}{\partial t} + a_k \frac{\partial \Phi}{\partial x_k} = 0, \tag{16}$$

where a_k is the velocity of the interface, in the k-th direction. The interface velocity a_k is obtained from solving the Riemann problem at the interface [15]. For Eq. 16, we implement Hamilton-Jacobi WENO for fifth order spatial accuracy in smooth flow and either second-order van Leer or total variation diminishing third-order Runge-Kutta (RK3) time integration [13]. The level set is initialized given the initial location of the interface. For distance d, which gives the shortest distance between an interface location (x_I, y_I, z_I), with subscript "I" denoting the interface location, and a level set point (x, y, z), the level set is defined as

$$\Phi(x, y, z) = \pm \min[d(x_I, y_I, z_I, x, y, z)], \tag{17}$$

where the negative sign is given for a point within the material region and positive sign otherwise. The surface $\Phi = 0$ indicates the boundary of the material.

D. Ghost fluid boundary conditions at material interface

For each material, the update is limited to the material regions defined by the level set Φ. In practice, ghost zones are necessary for spatial differencing and reconstruction stencils that extend beyond the indexed domain for each material. In GNARLYX, we implement constant extrapolation [25] for all primitive variables, defined by the level set $\Phi \leq 0$, extrapolated to the $\Phi > 0$ region and vice versa. This is done as a constant along a normal $\vec{n}$ to the interface, defined by the level set function,

$$\vec{n} = \frac{\vec{\nabla}\Phi}{|\vec{\nabla}\Phi|}. \tag{18}$$

For the extrapolation, we solve

$$H(\Phi)\vec{n} \cdot \vec{\nabla} u = 0, \tag{19}$$

where $H(\Phi)$ is the unit Heaviside function,

$$H(\Phi) = \begin{cases} 0, & \text{if } \Phi > 0 \\ 1, & \text{if } \Phi \leq 0 \end{cases}, \tag{20}$$

and specify $\vec{\nabla}$ with a fourth-order stencil. For materials without strength, we implement a contact discontinuity boundary condition, where the velocity and pressure are constant across the material interface. More generally, for materials with strength, we apply a traction equilibrium constraint, where the traction vector is constant across the surface. We define a stress vector or traction as $T_i = \sigma_{ij}\mathbf{e}_j$, in terms of the Cauchy stress σ and unit basis vector $\mathbf{e}_i$ The traction equilibrium constraint along a normal $\vec{n}$ to the interface equates the tractions on the left (L) and right (R) sides of the interface, where we have in 1D,

$$\sigma_{nn}^L = \sigma_{nn}^R. \tag{21}$$

If both of the materials are without strength, this reduces to the contact discontinuity

$$p^L = p^R. \tag{22}$$

There are a variety of methods to address the interface conditions above using approximate solutions to the Riemann problem [15, 26]. We implement an approximate solver based on solving the Rankine-Hugoniot conditions across a wave speed [15] because it addresses materials with and without strength in a general manner. We choose this method over a Primitive Variable Riemann Solver (PVRS) method because of convenience. The latter produces an approximate solution via characteristic equations. For hydrodynamics with a straightforward analytic EOS and materials without strength, the coefficient matrix for the primitive form of the Euler equations is constructed from easily obtainable eigenvectors. However, this method is not convenient for complicated EOS and materials with strength because the eigenvectors are difficult to obtain. Alternatively, for an approximate solver based on solving the Rankine-Hugoniot conditions, we only need the eigenvalues and these are straightforward to obtain. We have, as described in Sec. II B, a coefficient matrix based on the conservative form of the equation, where inversion for pressure and energy is not necessary (as for the primitive form) and avoided for complex EOS. Thus, for an approximate solver based on solving the Rankine-Hugoniot conditions across a wave speed [15], we solve

$$\bar{A}\Delta\mathcal{U} = \lambda\Delta\mathcal{U}, \tag{23}$$

where the coefficient matrix $\bar{A}$ is assumed to be constant with constant state $\mathcal{U} = \{\bar{\rho}, \bar{u}_1, \bar{\sigma}_{11}, \dots\}$ in 1D, for eigenvalue λ. In obtaining the traction equilibrium constraint in Eq. 21, we only need expressions using rows associated with ρ and u. We consider the longitudinal wave speeds given in Sec. II B, where $\lambda = u_1 \pm a$, for $a = c_{\text{long}}$. As in Toro [15], we use arithmetic averaging $\bar{\rho} = (\rho_L + \rho_R)/2$ and $\bar{a} = (a_L + a_R)/2$. We then solve the jump conditions defined by Eq. 23 which give a complete system of equations specified by the interface variables $\{\rho_L^*, \rho_R^*, u^* = u_L^* = u_R^*, \sigma_{11}^* = \sigma_{11,L}^* = \sigma_{11,R}^*\}$ in terms of the known variables left and right adjacent to the interface $\{\rho_L, \rho_R, u_L, u_R, \sigma_{11,L}, \sigma_{11,R}\}$ as well as $\bar{\rho}$ and $\bar{a}$. The 1D traction equilibrium conditions in the x-direction are then,

$$\rho_L^* = \frac{1}{2}\left[\bar{\rho}(u_L - u_R)/\bar{a} + (\sigma_{11,L} - \sigma_{11,R})/\bar{a}^2\right] + \rho_L, \tag{24}$$

$$\rho_R^* = \frac{1}{2}\left[\bar{\rho}(u_L - u_R)/\bar{a} + (\sigma_{11,R} - \sigma_{11,L})/\bar{a}^2\right] + \rho_R, \tag{25}$$

$$u^* = \frac{1}{2}\left[(\sigma_{11,R} - \sigma_{11,L})/(\bar{\rho}\bar{a}) + u_L + u_R\right], \tag{26}$$

$$\sigma_{11}^* = \frac{1}{2}\left[\bar{\rho}\bar{a}(u_R - u_L) + \sigma_{11,L} + \sigma_{11,R}\right]. \tag{27}$$

In practice, we use only the velocity and the stress (in 1D, we have u^* and σ_{11}^*) for the interface in replacing the quantities in the zones adjacent to the interface [26].

III. 1D VERIFICATION OF THE HYDROCODE GNARLYX

A. Constitutive models

In the following, we describe the EOS and hyperelastic, perfectly plastic constitutive models used in the 1D verification test for GNARLYX described below. We consider material models for PBX 9502 and aluminum.

1. Equation of State

We consider a Mie-Grüneisen EOS where the specific internal energy is given by

$$e_{\text{eos}} = e_{\text{int}}(\rho, p) = e_r(\rho) + \frac{1}{\rho\Gamma}[p - p_r(\rho)], \tag{28}$$

for reference curves $e_r(\rho)$ and $P_r(\rho)$. Re-writing Eq. 28, we have, for the pressure,

$$p_{\text{eos}} = p(\rho, e_{\text{eos}}) = \rho\Gamma[e_{\text{eos}} - e_r(\rho)] + p_r(\rho). \tag{29}$$

TABLE I: EOS parameters. Parameters of ambient density ρ_0, ambient sound speed c_0, coefficient s in the linear $u_s - u_p$ relation, and Grüneisen constant Γ for PBX 9502 and aluminum modeled as Mie-Grüneisen EOS with Hugoniot reference curve [27–30].

Material	ρ_0 [g/cm^3]	c_0 [km/s]	s	Γ
PBX 9502	1.89	2.4	2.05	1.1464
Al	2.79	5.33	1.34	2.0

TABLE II: Material strength parameters. PBX 9502 is not modeled with a strength model. Parameters are given for aluminum modeled as a hyperelastic, perfectly plastic material with constant shear modulus μ and yield Y [30].

Material	μ [GPa]	Y [GPa]
PBX 9502	N/A	N/A
Al	28.6	0.26

For a Hugoniot reference curve [27], we have

$$p_r(\rho) = \rho_0 c_0^2 \left(1 - \frac{\rho_0}{\rho}\right) \left[1 - s\left(1 - \frac{\rho_0}{\rho}\right)\right]^{-2}, \tag{30}$$

$$e_r(\rho) = \frac{P_r(\rho)}{2\rho_0} \left(1 - \frac{\rho_0}{\rho}\right), \tag{31}$$

parameterized by ambient density ρ_0, ambient sound speed c_0, coefficient in the linear $u_s - u_p$ relation s, and Grüneisen constant Γ. The EOS parameters for PBX 9502 and aluminum are given in Table I. While this is not a complete EOS [27], it is chosen for convenient comparison to the EOS models and solutions in [29, 30].

2. Hyperelastic, perfectly plastic strength

We consider a material strength model such that the Cauchy stress is evaluated in separable components in Eq. 8, with an EOS component which determines the hydrodynamic pressure p and an elastic component which determines the deviatoric stress τ [20–22, 30]. We assume a hyperelastic constitutive model, parameterized by a constant shear modulus

μ. We assume the deviatoric contribution to the Helmholtz free energy density is given by

$$\tilde{\rho}\Psi_{\text{dev}}(\hat{\mathbf{E}}_e) = \mu\hat{\mathbf{E}}_e : \hat{\mathbf{E}}_e, \tag{32}$$

for reference density $\tilde{\rho} = \rho_0$, where $\hat{\mathbf{E}}_e = \frac{1}{2}(\hat{\mathbf{F}}_e^T\hat{\mathbf{F}}_e - \mathbf{I})$ is the deviatoric part of the elastic Green-Lagrange strain and $\hat{\mathbf{F}}_e = (\text{det}\mathbf{F}_e)^{-1/3}\mathbf{F}_e$ is the deviatoric part of the deformation gradient $\mathbf{F}_e$. We define a generic stress as $\hat{S} = 2\mu\hat{\mathbf{E}}_e$. Then, the deviatoric contribution to the second Piola-Kirchhoff (PK2) stress in the immediate configuration is obtained by projection,

$$\tilde{S}_{\text{dev}} = \hat{S} : \mathbf{M} = \{\hat{S} - \frac{1}{3}[(\mathbf{C}_e : \hat{S})\mathbf{C}_e^{-1}]\}(\text{det}\mathbf{F}_e)^{-2/3}, \tag{33}$$

with projection operator $\mathbf{M} = (\text{det}\mathbf{F}_e)^{-2/3}(\mathbf{I}\boxtimes\mathbf{I} - \frac{1}{3}\mathbf{C}_e\otimes\mathbf{C}_e^{-1})$, where $\mathbf{C}_e = \mathbf{F}_e^T\mathbf{F}_e$ [20]. The deviatoric part of the Cauchy stress is then,

$$\tau(\mathbf{F}_e, \mu) = \frac{1}{\text{det}\mathbf{F}_e}\mathbf{F}_e\tilde{S}_{\text{dev}}\mathbf{F}_e^T, \tag{34}$$

by transformation into the current configuration using the elastic deformation gradient. From Eq. 32, the elastic internal energy density is given by

$$u_{\text{elastic}}(\mathbf{F}_e, \mu) = \rho e_{\text{elastic}} = \mu\hat{\mathbf{E}}_e : \hat{\mathbf{E}}_e. \tag{35}$$

We define the plastic source term as

$$\Omega^p = \mathbf{F}^e\mathbf{L}^p, \tag{36}$$

where $\mathbf{F}^e$ acts as a push-forward of the plastic distortion rate $\mathbf{L}^p$ into the current configuration. We define a plastic flow rule of the form [14, 20–22]

$$\mathbf{L}^p = \mathbf{N}\dot{\gamma}, \tag{37}$$

for slip rate $\dot{\gamma}$ and, for isotropic flow,

$$\mathbf{N} = (\mathbf{F}^e)^{-1}\frac{\tau}{\sigma_{\text{eq}}}\mathbf{F}^e, \tag{38}$$

where $\sigma_{\text{eq}} = \sqrt{\frac{3}{2}\tau : \tau}$ is the equivalent form of the Cauchy stress. We consider an isotropic, perfectly plastic model [30], parameterized by the yield Y. The plastic yield function is

$$f(\tilde{\sigma}_{\text{eq}}) = \tilde{\sigma}_{\text{eq}} - Y = 0, \tag{39}$$

for trial equivalent stress $\tilde{\sigma}_{\text{eq}}$. When $f \geq 0$ in Eq. 39, the stress is at or extends beyond the yield surface and the material undergoes plastic deformation. In general, plasticity models depend on how the yield function $f(\tilde{\sigma}_{\text{eq}})$ is incorporated into the slip rate $\dot{\gamma}$ in the plastic flow rule of Eq. 37. We consider a perfectly plastic update based on a radial return method to numerically calculate the slip rate for the source term. At each iteration, we calculate a trial equivalent stress $\tilde{\sigma}_{\text{eq}}$, obtained from a trial elastic deformation gradient $\overline{\mathbf{F}}_e$, and check if the yield function in Eq. 39 is satisfied. This is a root-finding scheme to obtain a slip rate $\dot{\gamma}$, where $f[\tilde{\sigma}_{\text{eq}}(\dot{\gamma})] = 0$ ensures that the plastic behavior occurs at the yield surface only.

B. 1D incident, reflected, transmitted shocks at the material interface of PBX 9502 and aluminum, modeled without strength

In 1D, consider the shock states resulting from an incident shock traveling left to right, impacting the material interface of PBX 9502 and aluminum, modeled without strength. This initial shock wave moves from low density PBX 9502 to high density (high shock impedance) aluminum, producing a reflected shock in PBX 9502 and transmitted shock in aluminum. The material interface, particle velocities in each of the states (incident, reflected, transmitted), and transmitted shock propagate in the direction of the incident shock. The reflected shock is directed in the opposite direction. We obtain the state quantities between the incident, reflected, transmitted shocks with shock velocities D_i, D_r, and D_t, respectively, given the incident shock speed D_i and the initial, ambient conditions for each material while enforcing the contact discontinuity (reduced traction equilibrium condition for materials without strength) boundary conditions at the material interface.

1. Exact solution for shock states

We consider Mie-Grüneisen EOS with Hugoniot reference curves in Sec. III A 1 for both materials with parameters given by Table I. The shock states are obtained from the Hugoniot jump conditions at each shock and the contact discontinuity connecting the reflected-

TABLE III: Exact solution for 1D incident, reflected, transmitted shocks at the material interface of PBX 9502 and aluminum. Aluminum is modeled without strength. Incident and reflected shock states are inside PBX 9502. Transmitted shock state is inside aluminum. The density ρ, pressure p, particle velocity u, and shock velocity D are given with high precision for direct comparison with numerical simulations to round-off error.

Shock state	ρ [g/cm^3]	p [GPa]	u [mm/μs]	D [mm/μs]
Incident	2.094324324324324	1.659512195121952	2.926829268292684e-1	3.0
Reflected	2.171422410559692	2.5895404181265955	1.671158637057647e-1	3.243839809444038
Transmitted	2.8765544629708284	2.5895404181265955	1.671158637057647e-1	5.553935257365725

transmitted states. The incident shock state in PBX 9502 is given by

$$\rho_i = \rho_0 \left[1 - \frac{1}{s}\left(1 - \frac{c_0}{D_i}\right)\right]^{-1} \tag{40}$$

$$p_i = \frac{\rho_0 D_i^2}{s}\left(1 - \frac{c_0}{D_i}\right), \tag{41}$$

$$u_i = \frac{D_i}{s}\left(1 - \frac{c_0}{D_i}\right), \tag{42}$$

for incident density ρ_i, pressure p_i, and velocity u_i in the x-direction. The reflected shock state is expressed in terms of the incident state, through the Hugoniot jump conditions across the reflected shock with direction $\vec{n}_r = -\vec{n}_i$, opposite to the particle velocity $\vec{n}_r \cdot \vec{u}_r = -u_r$. For mass conservation, we have

$$\rho_r(\vec{n}_r \cdot \vec{u}_r - D_r) = \rho_i(\vec{n_r} \cdot \vec{u}_i - D_r), \tag{43}$$

where $\vec{n_r} \cdot \vec{u}_i = (\vec{n}_r \cdot \vec{n}_i)(\vec{n}_i \cdot \vec{u}_i)$. The reflected density is then,

$$\rho_r = \rho_i \left(\frac{D_r + u_i}{D_r + u_r}\right). \tag{44}$$

For momentum conservation, we have

$$\rho_r(\vec{n}_r \cdot \vec{u}_r - D_r)^2 + p_r = \rho_i(\vec{n}_r \cdot \vec{u}_i - D_r)^2 + p_i. \tag{45}$$

The reflected pressure is then

$$p_r = \rho_i(u_i + D_r)^2 + p_i - \rho_r(u_r + D_r)^2. \tag{46}$$

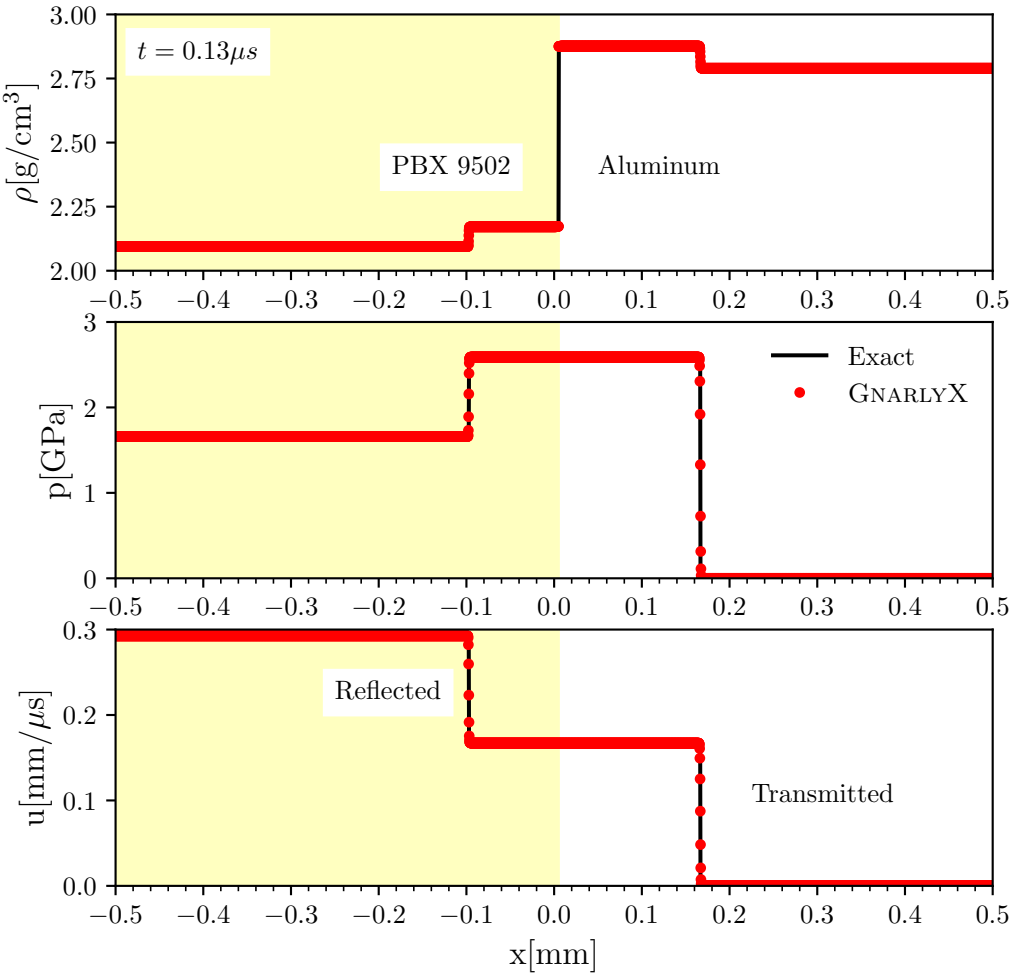

FIG. 1: Comparison of the exact (solid black line) and GNARLYX (dotted red line) solutions for the hydrodynamic profiles of density ρ, pressure p, and velocity u. Evolution at $t = 0.13\mu$s gives the reflected shock and the transmitted shock from the material interface of PBX 9502 and aluminum. The level set separates material regions into PBX 9502 (yellow) and aluminum (white).

From energy conservation, for specific internal energies e_i and e_r, we have

$$e_r + \frac{p_r}{\rho_r} + \frac{1}{2}(\vec{n}_r \cdot \vec{u}_r - D_r)^2 = e_i + \frac{p_i}{\rho_i} + \frac{1}{2}(\vec{n}_r \cdot \vec{u}_i - D_r)^2. \tag{47}$$

From Eq. 44, Eq. 46, Eq. 47, and EOS in Eq. 28, we have four equations and four independent unknowns $\{\rho_r, p_r, u_r, D_r\}$. We now add four more independent unknowns $\{\rho_t, p_t, u_t, D_t\}$ for the transmitted shock state and close the system of equations which specify all the states by connecting the reflected and transmitted shock states using the contact discontinuity. The equations for the transmitted shock state in aluminum are of similar form to the incident

shock state in PBX9502, where

$$\rho_t = \rho_0 \left[1 - \frac{1}{s}\left(1 - \frac{c_0}{D_t}\right)\right]^{-1} \tag{48}$$

$$p_t = \frac{\rho_0 D_t^2}{s}\left(1 - \frac{c_0}{D_t}\right), \tag{49}$$

$$u_t = \frac{D_t}{s}\left(1 - \frac{c_0}{D_t}\right), \tag{50}$$

for transmitted density ρ_t, pressure p_t, and velocity u_t in the x-direction. Combining Eq. 49 and Eq. 50, we have a convenient expression for the pressure in terms of the velocity,

$$p_t = \rho_0 u_t (c_0 + s u_t). \tag{51}$$

From the contact discontinuity at the material interface, we obtain two more equations, where the pressure and particle velocity are continuous such that,

$$u_r = u_t, \tag{52}$$

$$p_r = p_t. \tag{53}$$

Then, from Eq. 48, Eq. 51, Eq. 52, and Eq. 53, we have four equations that specify the transmitted state for a total of eight equations and eight unknowns to close the system of equations which specify all the states. The exact solution with incident shock speed $D_i = 3$ mm/μs is given in Table III.

2. *Verification with* GnarlyX

We compare the exact solution given in Sec. III B 1 with numerical simulations with GnarlyX using the following methods. From Athena++, we use the second-order van Leer time integration scheme for the hydrodynamic and level set update and the second-order piecewise linear spatial reconstruction for the primitive variables. We add fifth-order WENO spatial differencing for the level set update. For the Riemann solver, we add a Lax-Friedrichs method for multi-materials and condensed phase EOS. For the boundary condition extrapolation at the material interface, we add a constant extrapolation with a fourth-order stencil [25]. In comparing the exact and numerical solutions, we consider units convenient for HE applications. Detonation velocities occur at $\sim$ km/s and we use the equivalent unit of mm/μs for the velocity across a length scale of millimeters and time

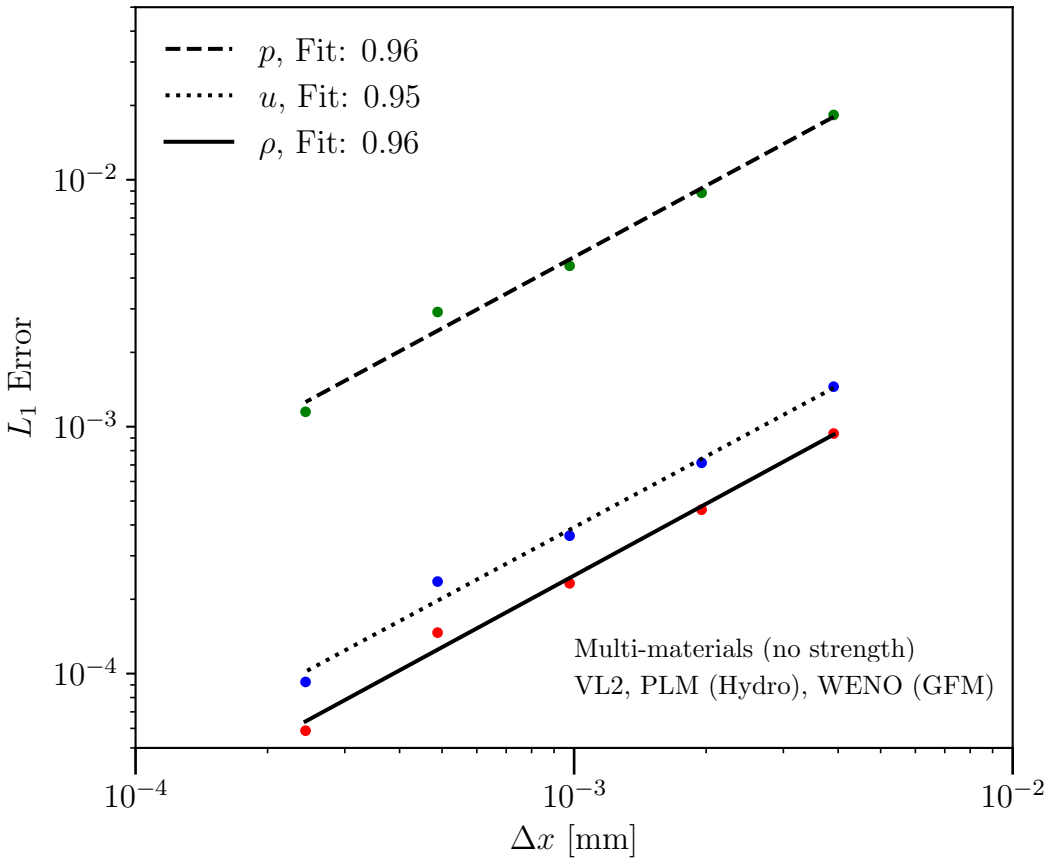

FIG. 2: Convergence study for GNARLYX in L_1 error versus spatial resolution. The convergence rates for density ρ, pressure p, and velocity u are close to order unity.

duration in microseconds. Density is in cgs units. Pressure is measured in GPa. For this test, we consider an incident shock speed at $D_i = 3$ mm/μs. This is significantly lower than the typical detonation speed in PBX 9502, ensuring that shock transmission into aluminum is under the Hugoniot elastic limit, leading to a split elastic-plastic wave [27, 31]. This impact velocity is relevant to HE safety applications. We now present the details of 1D verification simulations of a shock impacting the material interface of PBX9502 and aluminum. The length of the physical domain is $x = [-0.5, 0.5]$ mm. We resolve the computational domain with total number of zones $\{128, 256, 512, 1024, 2048, 4096\}$. The total time evolution is $t_f = 0.13\mu$s. The initial position of the incident shock is $x_{i,0} = -0.3$ mm. The initial position of the material interface (contact discontinuity) is $x_{c,0} = 0.0$ mm. The time of impact, when incident shock reaches the interface, is $t_{\text{impact}} = -x_{i,0}/D_i$. The position of the contact discontinuity $x_c = (t_f - t_{\text{impact}})u_r + x_{c,0}$, reflected shock $x_r = (t_f - t_{\text{impact}})D_r + x_{c,0}$,

and transmitted shock $x_t = (t_f - t_{\text{impact}})D_t + x_{c,0}$ depend on the initial choice of $x_{i,0}$ and $x_{c,0}$. Figure 1 shows density, pressure, and velocity profiles at $t_f = 0.13\mu$s, a point in the time evolution after the incident shock hits the material interface, producing a reflected shock wave traveling in the -x direction at x_r through PBX 9502 and a transmitted shock wave traveling in the +x direction at x_t through aluminum. The contact discontinuity also travels in the +x direction at x_c through aluminum, identified in Fig. 1 by the transition point between the yellow and white shading. The three panels show a comparison of the exact solution in the solid black line with the numerical result of GNARLYX at resolution $\Delta x = 2.4e-4$ mm in the red dotted line. GNARLYX captures the reflected shock and transmitted shock and maintains the contact discontinuity boundary condition, where there is a jump in density, but continuous in pressure and velocity across the material interface. We find that the numerical solution converges to the exact solution for all spatial resolutions considered. We consider a convergence study using the L_1 error defined for hydrodynamic variable $f = \{\rho, p, u\}$, where f_i is the numerical cell-centered value at index i, f_{exact} is the exact solution at position x_i, and Δx_i is the cell-width at x_i,

$$L_1 = \sum_i |f_i - f_{\text{exact}}|\Delta x_i. \tag{54}$$

Fig. 2 shows the L_1 error versus resolution size Δx for the three hydrodynamic profiles ρ, p, and u. GNARLYX produces convergence rates for each profile close to first-order as expected for shock-capturing methods.

C. 1D incident, reflected, transmitted split elastic-plastic shocks at the material interface of PBX 9502 and aluminum

Consider the previous set up in Sec. III B, where aluminum is modeled with strength. This initial shock wave moves from low density PBX 9502 to high density (high shock impedance) aluminum, producing a reflected shock in PBX 9502 and transmitted, split elastic-plastic shocks in aluminum. The split transmitted wave of an elastic precursor followed by a plastic shock wave results from the behavior of aluminum with material strength [31]. The material interface, particle velocities in each of the states (incident, reflected, transmitted elastic, and transmitted plastic), and transmitted shocks propagate in the direction of the incident shock. The reflected shock is directed in the opposite direction. We obtain the state quantities

TABLE IV: Exact solution for 1D incident, reflected, transmitted split elastic-plastic shocks at the material interface of PBX 9502 and aluminum. Aluminum is modeled with a hyperelastic, perfectly plastic model. Incident and reflected shock states are located inside PBX 9502. Transmitted elastic and plastic shocks states are located inside aluminum. The density ρ, pressure p, particle velocity u, and shock velocity D are given with high precision for direct comparison with numerical simulations to round-off error.

Shock state	ρ [g/cm^3]	p [GPa]	u [mm/μs]	D [mm/μs]
Incident	2.094324324324324	1.659512195121952	2.926829268292684e-1	3.0
Reflected	2.173721443525260	2.620590805610931	1.632162754677383e-1	3.251834042026332
Plastic	2.871736182750173	2.447257472277594	1.632162754677383e-1	5.589752109400773
Elastic	2.802749184157360	3.657742898480048e-1	2.964727041531747e-2	6.517582767917887

between the incident, reflected, transmitted elastic, and transmitted plastic shocks with shock velocities D_i, D_r, D_e, and D_p, respectively, given the incident shock speed D_i and the initial, ambient conditions for each material while enforcing the contact discontinuity boundary conditions at the material interface.

1. *Exact solution for shock states*

We use the same expressions for the incident and reflected shock states for the strengthless case given by Sec. III B 1. What remains for the solution is closing the full shock system using the contact discontinuity boundary condition, the transmitted elastic-plastic shock jump condition, and the jump condition between the elastic and ambient states. The transmitted elastic shock state $\{\rho_e, p_e, u_e, D_e\}$ is completely determined by the shear modulus μ and yield strength Y. We consider the finite strain uniaxial limit of a hyperelastic, perfectly plastic constitutive model [30]. The density at yield is

$$\rho_e = \frac{\rho_0}{F_{11}}. \tag{55}$$

We determine F_{11} by setting the value of the deviatoric stress τ in Eq. 34 at yield, where $\tilde{S}_{\text{dev}}$ is reduced to the uniaxial limit, and then solving

$$-\frac{2}{3}Y = \frac{2}{3}\mu(F_{11}^{7/3} - F_{11}^{-5/3} + F_{11}^{-1} - F_{11}). \tag{56}$$

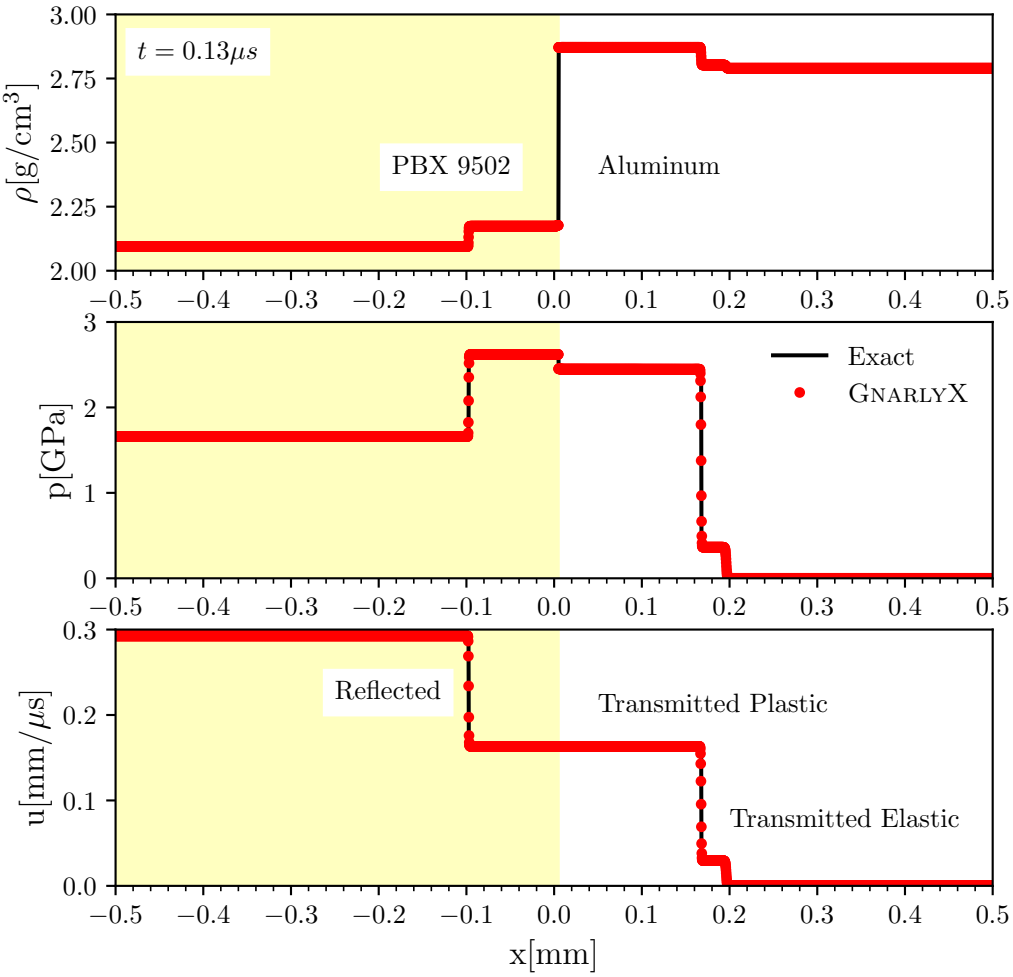

FIG. 3: Comparison of the exact (solid black line) and GNARLYX (dotted red line) solutions for the hydrodynamic profiles of density ρ, pressure p, and velocity u. Evolution at $t = 0.13\mu$s gives the reflected shock and the split transmitted precursor elastic shock followed by a plastic shock from the material interface of PBX 9502 and aluminum. The level set separates material regions into PBX 9502 (yellow) and aluminum (white).

The deviatoric stress at yield is then,

$$\tau_e = -\frac{2}{3}Y, \tag{57}$$

where $\sigma_e = -p_e + \tau_e$. From the mass and momentum jump conditions at the elastic shock, between the elastic and ambient states, we have the elastic shock velocity,

$$D_e^2 = \frac{\rho_e \sigma_e}{\rho_0(\rho_0 - \rho_e)}. \tag{58}$$

Combining the mass and energy jump conditions with the Mie-Grüneisen form of the EOS in Eq. 28, we have the specific internal energy at yield given by,

$$e_e = \frac{\left[p_r(\rho_e) - \rho_e \Gamma e_r(\rho_e) + \frac{2}{3}Y\right](\rho_e - \rho_0)}{2\rho_0\rho_e - \rho_e\Gamma(\rho_e - \rho_0)}., \tag{59}$$

which has EOS and elastic contributions, $e_e = e_{\text{e,EOS}} + e_{\text{e,elastic}}$. From the EOS in Eq. 29, the pressure is given by $p_e = p_{\text{eos}}(\rho_e, e_{\text{e,EOS}})$. Then, using the mass jump condition, the particle velocity at yield is

$$u_e = \frac{\rho_e - \rho_0}{\rho_e} D_e. \tag{60}$$

Using the jump conditions across the plastic shock, the plastic state $\{\rho_p, p_p, u_p, D_p\}$ is given in terms of the elastic state. From the mass jump condition, the plastic shock density is

$$\rho_p = \rho_e \frac{u_e - D_p}{u_p - D_p}. \tag{61}$$

In the elastic, perfectly plastic model, we assume the same deviatoric stress for the elastic and plastic states. Then, from the momentum jump condition, the plastic shock pressure is

$$p_p = p_e + \rho_e(D_p - u_e)(u_p - u_e). \tag{62}$$

Combining the mass and energy jump conditions with the Mie-Grüneisen form of the EOS in Eq. 28, the plastic specific internal energy is

$$e_p = e_e + \frac{1}{2}\frac{1}{\rho_e\rho_p}(p_e + p_p - 2\tau_e)(\rho_p - \rho_e), \tag{63}$$

which has EOS and elastic contributions, $e_p = e_{\text{p,EOS}} + e_{\text{p,elastic}}$, with $e_{\text{p,elastic}} = e_{\text{e,elastic}}$ due to the yield condition. For the plastic state, we have three equations in Eq. 61, 62, and 63 and four unknowns $\{\rho_p, p_p, u_p, D_p\}$. From the interface conditions, we obtain two more equations to close the total system of eight equations and eight unknowns, where the particle velocity and traction are continuous such that,

$$u_r = u_p, \tag{64}$$

$$p_r = p_p - \tau_e. \tag{65}$$

The exact shock states are given in Table III with high precision in order to directly compare with numerical simulations to round-off error.

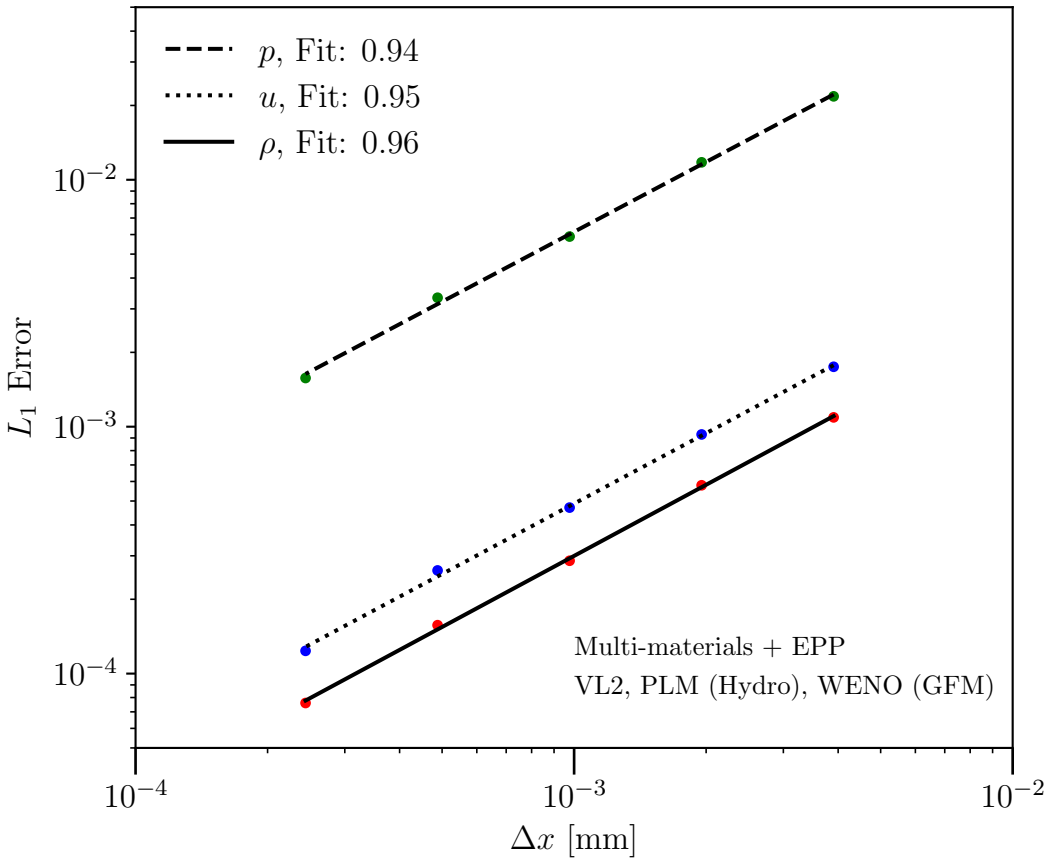

FIG. 4: Convergence study for GNARLYX in L_1 error versus spatial resolution. The convergence rates for density ρ, pressure p, and velocity u are close to order unity.

2. *Verification with* GNARLYX

We compare the exact solution given in Sec. III C 1 with numerical results by GNARLYX with methods and computational set up similar to Sec. III B 2. The position of the transmitted plastic shock $x_p = (t_f - t_{\text{impact}})D_p + x_{c,0}$ and transmitted elastic shock $x_e = (t_f - t_{\text{impact}})D_e + x_{c,0}$ depend on the initial choice of $x_{i,0}$ and $x_{c,0}$. Figure 3 shows density, pressure, and velocity profiles at $t_f = 0.13\mu$s, a point in the time evolution after the incident shock hits the material interface, producing a reflected wave traveling in the -x direction at x_r through PBX 9502 and a split transmitted wave traveling in the +x direction at x_p and x_e through aluminum. The contact discontinuity also travels in the +x direction at x_c through aluminum, identified in Fig. 3 by the transition point between the yellow and white shading. The three panels show a comparison of the exact solution in the solid black line with the numerical result of GNARLYX at resolution $\Delta x = 2.4e-4$ mm in the red dotted

line. GnarlyX captures the reflected shock and split transmitted elastic precursor shock followed by the plastic shock. It maintains the traction equilibrium boundary condition, where there is a jump in density, but continuous in traction and velocity across the material interface. Furthermore, we find that the numerical solution converges to the exact solution for all spatial resolutions considered. We consider a convergence study using the L_1 error defined in Eq. 54. Fig. 4 shows the L_1 error versus resolution size Δx for the three hydrodynamic profiles ρ, p, and u. GnarlyX produces convergence rates for each profile close to first-order as expected for shock-capturing methods.

IV. CONCLUSION

We present GnarlyX, a newly developed hydrocode for Eulerian multi-material hydrodynamics coupled to equation of state and hyperelastic, plastic constitutive models. These combined multi-material and strength capabilities are verified in 1D tests of the evolution of shock states resulting from an incident shock wave impacting the material interface of PBX 9502 and aluminum. We show in resolution studies that GnarlyX converges to the exact solution. While the verification tests presented here are at the macroscale, the multi-material and strength capabilities are also applicable to the mesoscale. In following work, we will present the thermomechanics and multi-dimensional, parallel computing capabilities in GnarlyX with multi-dimensional verification tests.

V. ACKNOWLEDGMENTS

We thank Marc Cawkwell (T-1) for fruitful discussions on the applications of GnarlyX to a variety of HE systems. We are grateful for support from Los Alamos National Laboratory (LANL) Advanced Simulation and Computing (ASC) program, Physics and Engineering Models (PEM) sub-program, operated by Triad National Security, LLC, for the National Nuclear Security Administration of U.S. Department of Energy (Contract No. 89233218CNA000001).

.

[1] C. Skidmore, D. Phillips, P. Howe, J. Mang, and J. Romero, Proc. 11th international detonation symposium), in *Proc. 11th International Detonation Symposium (Snowmass, Colorado, August - September 1998)* (1998).

[2] J. Ramsay and A. Popolato, Proc. 4th international detonation symposium, u. s. naval ordnance laboratory (u. s. government printing office, washington, d. c., 1965, in *Proc. 4th International Detonation Symposium, U. S. Naval Ordnance Laboratory (U. S. Government Printing Office, Washington, D. C.* (1998).

[3] R. Menikoff and T. D. Sewell, Constituent properties of HMX needed for mesoscale simulations, Combustion Theory and Modelling **6**, 103 (2002).

[4] G. Miller and P. Colella, A high-order eulerian godunov method for elastic–plastic flow in solids, Journal of Computational Physics **167**, 131 (2001).

[5] S. L. Gavrilyuk, N. Favrie, and R. Saurel, Modelling wave dynamics of compressible elastic materials, J. Comput. Phys. **227**, 2941 (2008).

[6] P. Barton, D. Drikakis, E. Romenski, and V. Titarev, Exact and approximate solutions of riemann problems in non-linear elasticity, Journal of Computational Physics **228**, 7046 (2009).

[7] P. T. Barton, D. Drikakis, and E. I. Romenski, An eulerian finite-volume scheme for large elastoplastic deformations in solids, International Journal for Numerical Methods in Engineering **81**, 453 (2010), https://onlinelibrary.wiley.com/doi/pdf/10.1002/nme.2695.

[8] Favrie, N. and Gavrilyuk, S., Dynamics of shock waves in elastic-plastic solids, ESAIM: Proc. **33**, 50 (2011).

[9] Favrie, N. and Gavrilyuk, S., Mathematical and numerical model for nonlinear viscoplasticity, Philosophical Transactions of the Royal Society A: Mathematical, Physical and Engineering Sciences **369** (2011).

[10] P. Barton, B. Obadia, and D. Drikakis, A conservative level-set based method for compressible solid/fluid problems on fixed grids, Journal of Computational Physics **230**, 7867 (2011).

[11] T. D. Aslam, J. B. Bdzil, and D. Stewart, Level set methods applied to modeling detonation shock dynamics, Journal of Computational Physics **126**, 390 (1996).

[12] R. P. Fedkiw, T. Aslam, B. Merriman, and S. Osher, A Non-oscillatory Eulerian Approach

to Interfaces in Multimaterial Flows (the Ghost Fluid Method), Journal of Computational Physics **152**, 457 (1999).

[13] S. Osher, R. Fedkiw, and K. Piechor, Level Set Methods and Dynamic Implicit Surfaces, Applied Mechanics Reviews **57**, B15 (2004).

[14] P. Barton, R. Deiterding, D. Meiron, and D. Pullin, Eulerian adaptive finite-difference method for high-velocity impact and penetration problems, Journal of Computational Physics **240**, 76 (2013).

[15] E. F. Toro, *Riemann Solvers and Numerical Methods for Fluid Dynamics* (Springer, Berlin, 1999).

[16] J. M. Stone, T. A. Gardiner, P. Teuben, J. F. Hawley, and J. B. Simon, Athena: A New Code for Astrophysical MHD, The Astrophysical Journal Supplements **178**, 137 (2008), arXiv:0804.0402.

[17] C. J. White, J. M. Stone, and C. F. Gammie, An Extension of the Athena++ Code Framework for GRMHD Based on Advanced Riemann Solvers and Staggered-mesh Constrained Transport, The Astrophysical Journal Supplements **225**, 22 (2016), arXiv:1511.00943 [astro-ph.HE].

[18] K. G. Felker and J. M. Stone, A fourth-order accurate finite volume method for ideal MHD via upwind constrained transport, Journal of Computational Physics **375**, 1365 (2018), arXiv:1711.07439 [astro-ph.IM].

[19] J. M. Stone, K. Tomida, C. J. White, and K. G. Felker, The Athena++ Adaptive Mesh Refinement Framework: Design and Magnetohydrodynamic Solvers, The Astrophysical Journal Supplement Series **249**, 4 (2020), arXiv:2005.06651 [astro-ph.IM].

[20] D. J. Luscher, C. A. Bronkhorst, C. N. Alleman, and F. L. Addessio, A model for finite-deformation nonlinear thermomechanical response of single crystal copper under shock conditions, Journal of the Mechanics and Physics of Solids **61**, 1877 (2013).

[21] D. Luscher, F. Addessio, M. Cawkwell, and K. Ramos, A dislocation density-based continuum model of the anisotropic shock response of single crystal α-cyclotrimethylene trinitramine, Journal of the Mechanics and Physics of Solids **98**, 63 (2017).

[22] D. J. Luscher, M. A. Buechler, D. J. Walters, C. Bolme, and K. J. Ramos, On computing the evolution of temperature for materials under dynamic loading, International Journal of Plasticity **111**, 188 (2018).

[23] E. F. Toro, M. Spruce, and W. Speares, Restoration of the contact surface in the hll-riemann

solver, Shock Waves **4**, 25 (1994).

[24] V. A. Titarev, E. Romenski, and E. F. Toro, Musta-type upwind fluxes for non-linear elasticity, International Journal for Numerical Methods in Engineering **73**, 897 (2008), https://onlinelibrary.wiley.com/doi/pdf/10.1002/nme.2096.

[25] T. Aslam, S. Luo, and H. Zhao, A static pde approach for multidimensional extrapolation using fast sweeping methods, SIAM Journal on Scientific Computing **36**, A2907 (2014), https://doi.org/10.1137/140956919.

[26] T. Liu, B. Khoo, and K. Yeo, Ghost fluid method for strong shock impacting on material interface, Journal of Computational Physics **190**, 651 (2003).

[27] R. Menikoff, Empirical equations of state for solids, in *ShockWave Science and Technology Reference Library*, edited by Y. Horie (Springer Berlin Heidelberg, Berlin, Heidelberg, 2007) pp. 143–188.

[28] S. P. Marsh, ed., LASL Shock Hugoniot Data (University of California Press, Berkeley, 1980).

[29] H. Udaykumar, L. Tran, D. Belk, and K. Vanden, An eulerian method for computation of multimaterial impact with eno shock-capturing and sharp interfaces, Journal of Computational Physics **186**, 136 (2003).

[30] E. J. Lieberman, X. Liu, N. R. Morgan, D. J. Luscher, and D. E. Burton, A higher-order lagrangian discontinuous galerkin hydrodynamic method for solid dynamics, Computer Methods in Applied Mechanics and Engineering **353**, 467 (2019).

[31] R. Menikoff, Elastic–plastic shock waves, in *ShockWave Science and Technology Reference Library*, edited by Y. Horie (Springer Berlin Heidelberg, Berlin, Heidelberg, 2007) pp. 189–224.